ARTICLES
PUBLISHED ONLINE: 21 AUGUST 2011 | DOI: 10.1038/NMAT3093
nature materials

A 3.90 V iron-based fluorosulphate material for lithium-ion batteries crystallizing in the triplite structure

P. Barpanda[1,2], M. Ati[1,2], B. C. Melot[1,2], G. Rousse[3], J-N. Chotard[1], M-L. Doublet[4], M. T. Sougrati[4], S. A. Corr[2,5], J-C. Jumas[4] and J-M. Tarascon[1,2,6]*

Li-ion batteries have empowered consumer electronics and are now seen as the best choice to propel forward the development of eco-friendly (hybrid) electric vehicles. To enhance the energy density, an intensive search has been made for new polyanionic compounds that have a higher potential for the Fe^{2+}/Fe^{3+} redox couple. Herein we push this potential to 3.90 V in a new polyanionic material that crystallizes in the triplite structure by substituting as little as 5 atomic per cent of Mn for Fe in $Li(Fe_{1-\delta}Mn_{\delta})SO_4F$. Not only is this the highest voltage reported so far for the Fe^{2+}/Fe^{3+} redox couple, exceeding that of $LiFePO_4$ by 450 mV, but this new triplite phase is capable of reversibly releasing and reinserting 0.7–0.8 Li ions with a volume change of 0.6% (compared with 7 and 10% for $LiFePO_4$ and $LiFeSO_4F$ respectively), to give a capacity of ~125 mA h g^{-1}.

Lithium-ion batteries continue to gain scientific and commercial importance in the present age of portable electronics and electric transportation. This drives researchers and engineers to build better batteries by optimizing several factors, including the energy density, rate capability, economy, safety and sustainability[1,2]. To achieve this goal, there has been an intensive search for new materials with promising electrochemical capacity for use as positive electrodes. Such efforts have resulted in the discovery of many new polyanionic systems, such as borate ($LiMBO_3$; ref. 3) silicate (Li_2MSiO_4; refs 4,5) pyrophosphate ($Li_2MP_2O_7$; ref. 6) and fluorophosphate ($LiMPO_4F$; ref. 7) compounds. The most significant benefit offered by these materials lies in the flexibility to increase the open-circuit voltage by manipulation of the 3*d*-metal $M^{n+}/M^{(n+1)+}$ redox couple through the electronic effects of the polyanion[8]. Employing this strategy, we previously reported the synthesis and structure of $LiFeSO_4F$, a 3.60 V cathode having a reversible capacity of ~140 mA h g^{-1} with good rate capability[9]. This was followed by the discovery of other isostructural fluorosulphates and their solid solutions ($LiMSO_4F$, M = Co, Ni; ref. 10), all of which have the triclinic $P\bar{1}$ tavorite structure, as illustrated in Fig. 1c.

During the course of the investigation of this fluorosulphate family, it was found that $LiMnSO_4F$ did not adopt the tavorite structure but instead was isostructural to the mineral triplite, $(Mn^{II}, Fe^{II}, Mg^{II}, Ca^{II})_2(PO_4)(F, OH)$ (ref. 11) and failed to show any electrochemical activity. This was particularly unusual given that all other examples of Li-based polyanionic compounds are known to be isostructural between Fe and Mn homologues ($LiMnPO_4$, Li_2MnSiO_4, $LiMnBO_3$, $Li_2MnP_2O_7$, $LiMnPO_4F$) and tend to demonstrate redox potentials much greater than their Fe-based counterparts.

To shed light on this surprising behaviour, we investigated the $Li(Fe_{1-\delta}Mn_{\delta})SO_4F$ solid solution and, in particular, the role Mn plays in the tavorite–triplite structural stability and electrochemical activity. Herein, we use synchrotron X-ray and neutron diffraction to present a thorough structural characterization of the triplite phase. The most fascinating discovery, however, is that substitutions as small as 5 atomic% of Mn can force $Li(Fe_{1-\delta}Mn_{\delta})SO_4F$ to crystallize in the same triplite structure with a corresponding increase in the Fe^{2+}/Fe^{3+} potential to 3.90 V: the highest value reported so far. *In situ* X-ray absorption near-edge structure (XANES) and Mössbauer spectroscopy are used to demonstrate that Mn is present solely as a spectator ion and is not oxidized at any attainable voltage using traditional electrolytes. We also show that within the Mn concentration range of $0 \leq \delta \leq 0.2$, the energetic stability of the tavorite versus triplite phases is, in fact, so close that either phase may be obtained depending on the precise reaction conditions. Such a result supports the idea that electrodes with the best performances tend to be those on the verge of structural instability.

Alkali metal fluorosulphate compounds ($AMSO_4F$; A represents Li/Na and M represents 3*d* metals) can be synthesized at a low temperature ($T \leq 300\,^{\circ}C$) through reaction of LiF with the corresponding 3*d*-metal monohydrate ($MSO_4 \cdot H_2O$). Syntheses have exploited ionothermal[9,10,12], solid-state[13–15] and polymer-assisted routes[16]. In this work, $LiMnSO_4F$ was synthesized at 295 °C using either an ionothermal (wet route involving 1-ethyl-3-methylimidazolium *bis*(trifluoromethane-sulphonyl)imide, EMI-TFSI, as the reaction media)[10] or solid-state preparation (where stoichiometric ratios of the starting materials were pressed into a pellet and sealed in a Teflon-lined autoclave filled with Ar) with reaction times of 24 and 48 h, respectively. Independent of

[1]Laboratoire de Réactivité et Chimie des Solides, CNRS UMR 6007, Université de Picardie Jules Verne, 80039 Amiens, France, [2]ALISTORE-European Research Institute, 80039 Amiens, France, [3]Institut de Minéralogie et de Physique des Milieux Condensés, CNRS UMR 7590, Université Pierre et Marie Curie, 4 Pl. Jussieu, 75252 Paris Cedex 5, France, [4]Institut Charles Gerhardt, CNRS UMR5253, Université Montpellier 2, 34 095 Montpellier, France, [5]School of Physical Sciences University of Kent, Canterbury CT2 7NH, UK, [6]Collège de France, 11 Place Marcelin Berthelot, 75005 Paris, France.
*e-mail: jean-marie.tarascon@sc.u-picardie.fr.

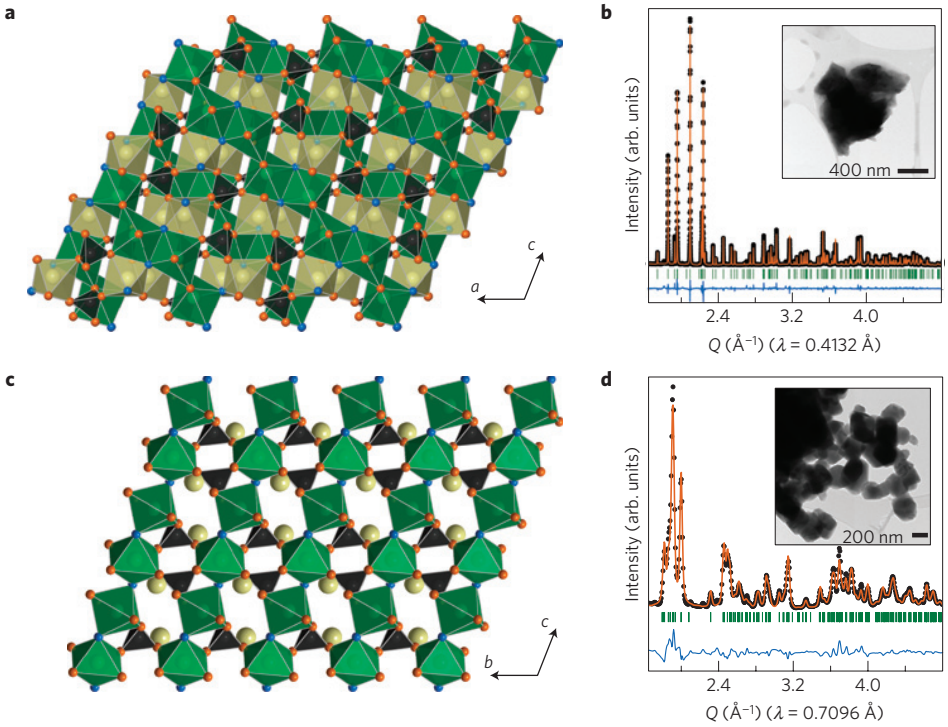

Figure 1 | Crystal structure and diffraction patterns of the tavorite and triplite phases. a–d, Illustration of the crystal structure of the triplite (**a**) and tavorite (**c**) structure type, and results of the Rietveld refinement of $Li(Fe_{0.9}Mn_{0.1})SO_4F$ in the triplite (**b**) and tavorite (**d**) structure against synchrotron XRD patterns. In **b** and **d**, the black dots correspond to observed data, the orange lines are the calculated patterns, the blue lines show the difference between the calculated and observed patterns and the vertical green bars correspond to the expected positions of the Bragg reflections ($R_{Bragg} = 5.56\%$ and 5.19%, respectively). The insets in **b** and **d** show TEM images of the powders prepared through the solid-state (**b**) and ionothermal (**d**) route.

the reaction method, a single-phase white powder of $LiMnSO_4F$ was recovered. The crystal structure of $LiMnSO_4F$ was refined against powder synchrotron X-ray diffraction (XRD) data using the Rietveld method as implemented in the FullProf software suite[17]. The resulting structure was found to crystallize in the monoclinic space group $C2/c$ with the lattice parameters and atomic positions that can be found in Supplementary Table S1.

As is the case for other fluorosulphates, the structure of triplite, illustrated in Fig. 1a, is composed of metal sites that are octahedrally coordinated by four tetrahedral SO_4 groups and two fluorine atoms. When compared with the tavorite structure, illustrated in Fig. 1c, triplite presents several important differences. First the triplite structure contains edge-sharing chains of MO_4F_2 octahedra, whereas tavorite consists of corner-sharing chains. This edge-sharing connectivity produces two crystallographically unique chains running along the [101] or [010] direction, which is distinct from the single chain in tavorite that has two unique crystallographic sites along the length of the chain. Furthermore, the F atoms in triplite lie in a *cis* orientation rather than the *trans* configuration found in tavorite. Also unlike $LiFeSO_4F$, the Li atoms in $LiMnSO_4F$ do not have a unique position, but instead are randomly distributed between the two metal sites, giving a relative occupancy of 50% Li and 50% Mn. It is important to note that this final point implies that Li will have a six-fold coordinate in triplite, which is expected to be far more stable when compared with the three-fold coordinate in tavorite.

To gain a better insight into this structural relationship between tavorite $LiFeSO_4F$ and triplite $LiMnSO_4F$, we attempted to prepare a solid solution of $Li(Fe_{1-\delta}Mn_\delta)SO_4F$. A priori, there were several outstanding questions. If such a solid solution could actually be prepared, it was not clear which structure would be more stable, and more importantly, it was unclear whether the electrochemical properties with respect to Li could be improved.

$Li(Fe_{1-\delta}Mn_\delta)SO_4F$ was prepared by reacting stoichiometric amounts of a mixed-metal sulphate monohydrate precursor $(Fe_{1-\delta}Mn_\delta)SO_4 \cdot H_2O$ with LiF. This monohydrate precursor was prepared in-house from commercial $FeSO_4 \cdot 7H_2O$ and $MnSO_4 \cdot H_2O$, as reported previously[10]. The same protocol of heating at 295 °C for 24 h or 2–3 days was used for the ionothermal and solid-state syntheses, respectively. Interestingly, all of the samples made using the solid-state approach, consisting of micrometre-size particles, as shown in the inset of Fig. 1b, could be fully indexed in the triplite unit cell (see Fig. 1b and Supplementary Tables S2 and S3). These samples showed a gradual shift of the Bragg peaks with increasing Mn content (Fig. 2a) that corresponds to an increasing unit-cell volume, as expected because the ionic radius of Mn^{2+} (0.830 Å) is greater than that of Fe^{2+} (0.780 Å; ref. 18). Such a smooth and linear increase in the volume signifies that a complete solid solution of $Li(Fe_{1-\delta}Mn_\delta)SO_4F (0.05 \leq \delta \leq 1)$ in the triplite phase could be obtained. In contrast, the ionothermal approach was found to yield nanometric powders, shown in the inset of Fig. 1d, whose XRD pattern (Fig. 1d) is indicative of the tavorite structure for $0 \leq \delta \leq 0.2$, with lattice parameters as reported in Supplementary Table S4. Samples prepared using the ionothermal method with compositions where $\delta > 0.2$ resulted in multiphase powders with $MnSO_4$ as the main impurity phase. To further evaluate the extent of cation disorder in the triplite phases, the structure of each sample in the triplite-phase $Li(Fe_{1-\delta}Mn_\delta)SO_4F$ solid solution was carefully refined against the laboratory and synchrotron powder XRD patterns. These refinements reveal that Li prefers to occupy the Wyckoff position we refer to as metal site 2, as illustrated in Fig. 2b.

Mössbauer spectroscopy was used to probe the disorder associated with Fe in both phases. Spectra were collected for Fe-rich polymorphs ($\delta = 0.05 - 0.2$) made both by the solid-state or ionothermal route. Regardless of the sample, all spectra show signatures of Fe^{2+} with no Fe^{3+} present within the error of the

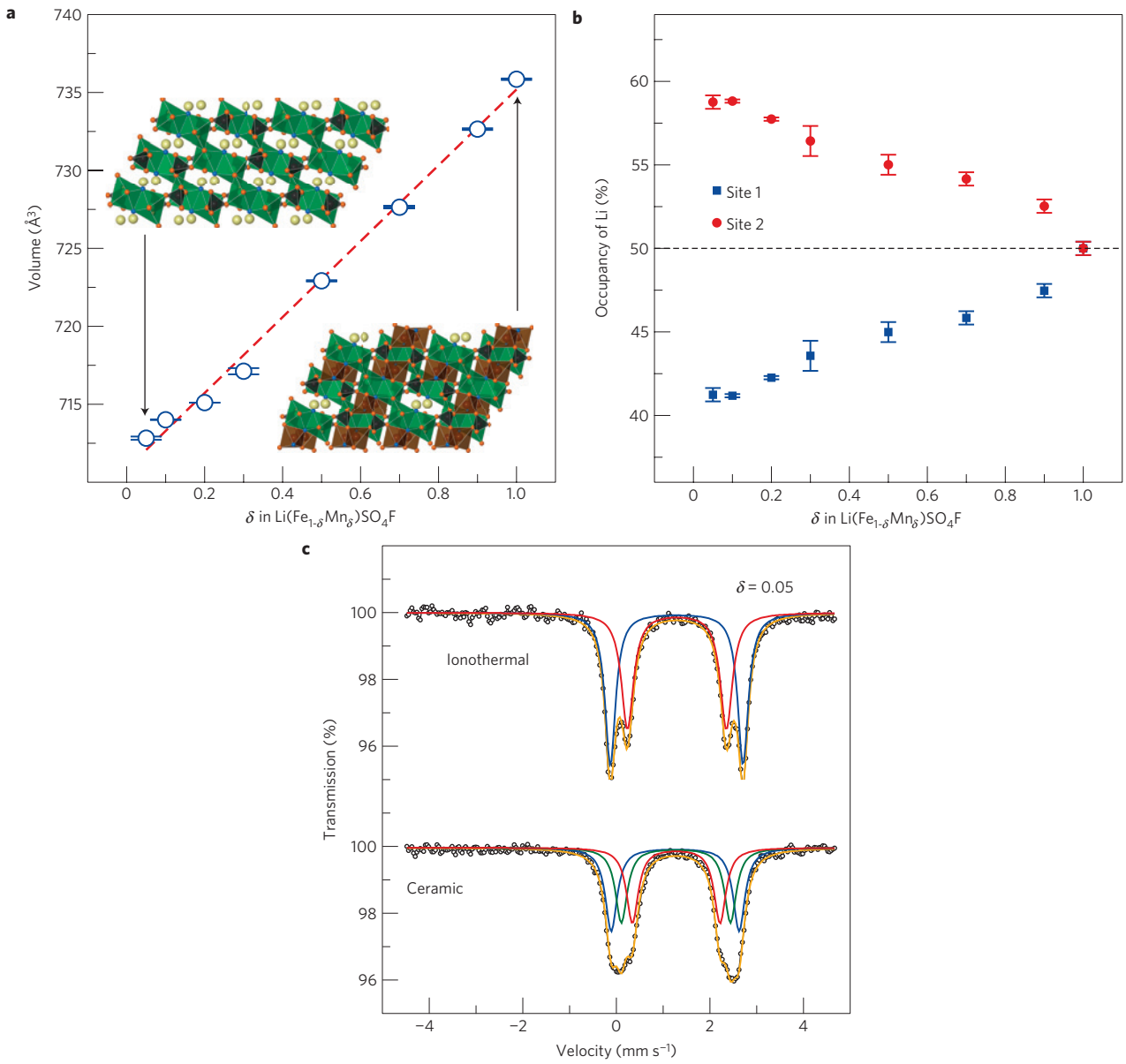

Figure 2 | Structural changes on Mn substitution. a, Unit-cell volume of the triplite phase with increasing substitution of Mn for Fe. As expected, there is a nearly linear increase of the unit-cell volume with increasing Mn content in the solid solution. The insets show two possible structures if the sites were to be fully segregated or completely random. **b**, Occupancy of Li on sites 1 and 2 of the triplite structure. Note that increasing Mn concentration results in an increasing degree of mixed site occupancy. **c**, Room-temperature Mössbauer spectra obtained for ionothermal/tavorite (top) and ceramic/triplite (bottom) samples for $\delta = 0.05$. The tavorite-phase spectrum can satisfactorily be fitted with two doublets, whereas three doublets, corresponding to three different Fe environments, are needed to fit the triplite-phase spectra.

measurements (see Supplementary Table S5). Some differences are seen between the two polymorphs. For instance, the tavorite-phase samples show two sharp sets of peaks (Fig. 2c top spectra) corresponding to the two distinct Fe1 and Fe2 crystallographic sites of MO_4F_2 octahedra within the chains, in agreement with that previously reported for $LiFeSO_4F$ (ref. 13), whereas the triplite samples (Fig. 2c bottom spectra) exhibit non-resolved and broadened peaks. In the latter, three types of Fe^{2+} environment, all having corresponding Mössbauer parameters in the range of paramagnetic high-spin Fe^{2+}, were necessary to successfully fit the triplite-phase spectra. Moreover, the quadrupole splitting was found to significantly decrease ($\sim$0.6 mm s^{-1}) with increasing Mn content, indicating an increasing distortion of the iron sites[19]. Overall, the observed peak broadening for triplite indicates multiple Fe^{2+} environments, confirming the disorder observed in the $LiMnSO_4F$ endmember. Such an observation from an average structural point of view would seem to preclude the possibility of a coherent pathway for Li-ion diffusion and hence may lead to little or no electrochemical activity.

To investigate the electrochemical performance, the voltage–composition traces for the 10% and 20% Mn-substituted tavorite and triplite-phase samples were collected. The tavorite-phase $Li(Fe_{0.9}Mn_{0.1})SO_4F$ (Fig. 3a) shows electrochemical activity around 3.60 V similar to the $LiFeSO_4F$ endmember[9]. It should be noted, however, that there is a slight loss of initial capacity with increasing Mn content because Mn is not electrochemically active.

The most spectacular result is found in the voltage–composition curve for the triplite-phase $Li(Fe_{0.9}Mn_{0.1})SO_4F$ cell (Fig. 3b), which demonstrates a reversible capacity of 0.7–0.8 Li^+ during the first charge–discharge cycle at an unexpected voltage of 3.90 V:

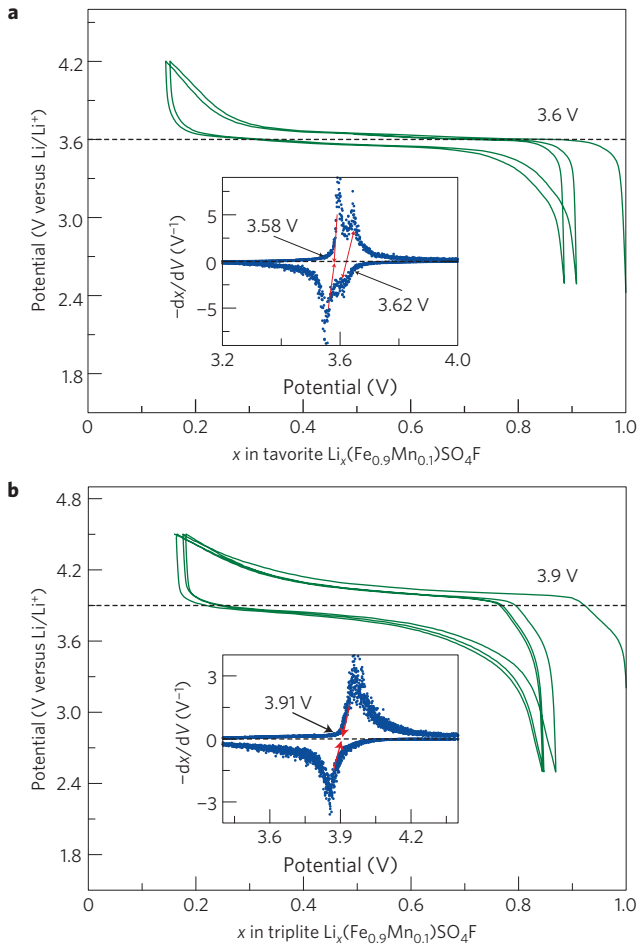

Figure 3 | Voltage–composition curves for the tavorite and triplite phases. **a**,**b**, Charge and discharge curves for tavorite (**a**) and triplite (**b**) phase $Li(Fe_{0.9}Mn_{0.1})SO_4F$ discharge at a C/20 rate. Note that the plateau of the redox potential is increased from 3.60 V in tavorite to 3.90 V in triplite for the same composition. The derived curves ($-dx/dV$) are plotted as a function of V. From their shapes (see text) and relative positions of the oxidation and reduction peaks, we can distinguish between single-phase (bell-shaped peaks) and two-phase insertion processes (asymmetric peaks).

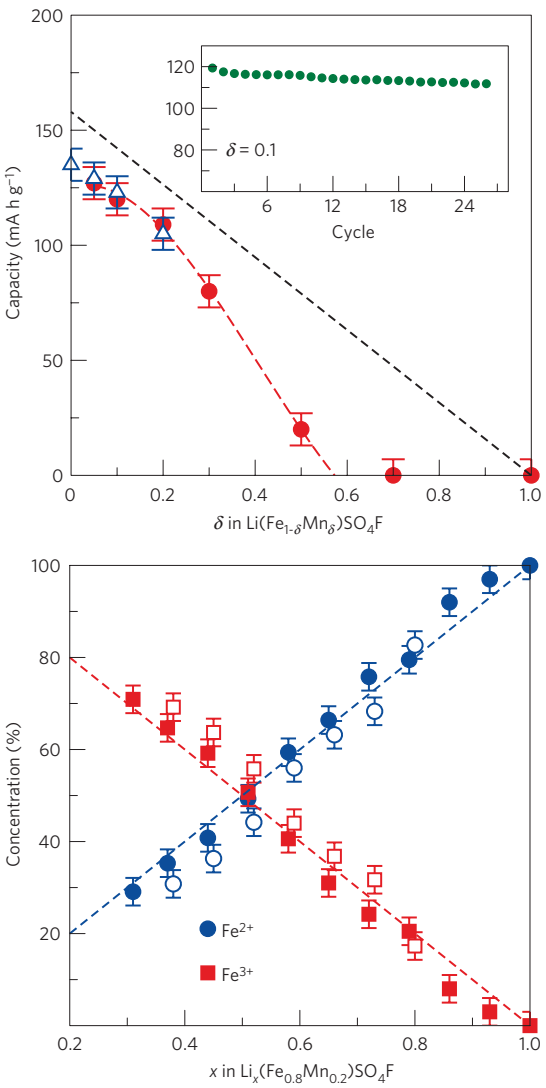

Figure 4 | Changes in electrochemistry with Mn substitution. a, Plot of capacity as a function of δ for $Li(Fe_{1-\delta}Mn_{\delta})SO_4F$ in both the tavorite (open blue triangles) and triplite (filled red circles) phases. The black dashed line is indicative of the expected reduction in capacity assuming that Mn is electrochemically inactive. At first, the capacity decreases linearly following the black dashed line and then deviates significantly, with the red dashed line acting as a guide to the eye. Independent of the decrease in capacity, the electrochemical activity remains centred at 3.90 V and 3.60 V for the triplite and tavorite phases. The inset shows the capacity retention on extended cycling at a rate of C/20 for the triplite phase of $Li(Fe_{0.9}Mn_{0.1})SO_4F$. **b**, Concentration of Fe^{2+} and Fe^{3+} oxidation states as determined by Mössbauer spectroscopy for an *in situ* $Li_x(Fe_{0.8}Mn_{0.2})SO_4F$/Li cell being charged (filled symbols) and discharged (open symbols) at a C/20 rate. The dashed lines correspond to the expected values for the amount of Li removed, and illustrate the good agreement, confirming the spectator role of Mn with respect to the Li-insertion–deinsertion process.

the highest Fe^{2+}/Fe^{3+} redox voltage ever reported so far for any inorganic compound. This high potential was confirmed by galvanostatic intermittent titration technique measurements (see Supplementary Fig. S1c). Furthermore, the alignment of the initial slopes of the oxidation and reduction peaks in the derivative curve for the triplite phase (inset of Fig. 3b) indicates unambiguously the presence of a first-order phase transition occurring at 3.910(5) V, with the long tail ending the reduction peak indicative of slow kinetics. Regarding the tavorite phase, shown as the inset of Fig. 3a, we first note the presence of a first-order phase transition between $0.8 < x < 1.0$ Li content occurring at 3.58 V, followed by a solid-solution domain centred at 3.62 V, as indicated by the large potential overlap of the second set of oxidation and reduction peaks. Finally, long-time cycling data show charge/discharge curves that neatly superimpose on each other to produce a steady capacity retention of roughly 120 mA h g^{-1} in $Li(Fe_{0.9}Mn_{0.1})SO_4F$ (inset of Fig. 4a). It should be noted that cells that contain electrodes based on the triplite phase show larger polarization (Fig. 3b) than their tavorite-based counterparts, indicating that the kinetics of the insertion–extraction process are slower for triplite. Such a result is not surprising given the intersite mixing found in the triplite phase.

To gain further insight into the insertion–extraction mechanism, *in situ* XRD measurements were carried out (see Supplementary Fig. S2). As a cell of $Li_x(Fe_{0.9}Mn_{0.1})SO_4F$ was being charged, we initially noted minor changes in the position and intensity of the peaks until the removal of 0.4 Li ($x = 0.6$). Beyond that value, marked changes occur in the range of 2θ between 28° and 32° in the powder pattern on decreasing x to 0.4, indicating the presence of a structural phase transition reminiscent of a two-phase Li insertion–extraction

process, in perfect agreement with the electrochemical data. A reversal of the peak shifts was found on discharge, indicating the full reversibility of the process, as confirmed by the remarkable similarity of the XRD patterns for the pristine electrode and the charged–discharged electrode. Furthermore, no changes were found in the XRD powder pattern for samples that had been cycled for more than 20 cycles. Last, *in situ* Mössbauer measurements were collected on $Li(Fe_{0.8}Mn_{0.2})SO_4F$ using a special electrochemical cell that was designed in-house. These data indicate the progressive oxidation of Fe^{2+} to Fe^{3+} on charging and its full conversion back to Fe^{2+} on discharging (Fig. 4b), further confirming the reversibility of the insertion–extraction process. Typical Mössbauer spectra obtained during the electrochemical cycling are given in the Supplementary Information (Supplementary Fig. S3 and Table S6).

To obtain further structural information on the fully delithiated phase, $Li_{0.25}(Fe_{0.8}Mn_{0.2})SO_4F$ was prepared through chemical oxidation from $Li(Fe_{0.8}Mn_{0.2})SO_4F$ by treatment with a solution of NO_2BF_4 and acetonitrile overnight. The compositions of the delithiated phases were confirmed using inductively coupled plasma measurements. The synchrotron powder diffraction pattern of the resulting sample (Fig. 5) closely resembled those made electrochemically but was free of the contribution from the beryllium window present in the *in situ* cell (Supplementary Fig. S2). The observed diffraction peaks could be fully indexed in a triplite cell of space group $C2/c$ with the lattice parameters given in Supplementary Table S7 and a unit cell volume, $V = 710.73(3)$ Å^3. Refinement of the structure against this high-resolution data leads to a volume change, $\Delta V/V$, of 0.6% between the lithiated ($V = 715.103(3)$ Å^3) and delithiated triplite phases, compared with 10.4% and 6.6% for $LiFeSO_4F/FeSO_4F$ and $LiFePO_4/FePO_4$ respectively. Such a result makes the triplite phase attractive with respect to industrial application, as there should be very little mechanical stress on extended cycling, which should allow for longer product lifetimes.

Regarding samples with a higher Mn content, we find a decrease in the overall capacity that should be expected assuming that the Mn ions are electrochemically inactive (Fig. 4a). For δ greater than 0.3, the capacity rapidly deviates from a linear relation between capacity and Mn concentration to reach zero for $\delta = 0.6$, indicating a structural hindrance for higher Mn content, which will be discussed in detail later. The role of Mn as a spectator ion, although indirectly proved by the capacity decay with increasing Mn content, was further confirmed by XANES measurements, which show no change in the K-edge of Mn with extraction of Li, whereas there is a significant shift in the K-edge of Fe (see Supplementary Figs S6 and S7).

In addition to being rich in practical importance, the results reported here raise important fundamental questions regarding the role of Mn in enhancing the Fe^{2+}/Fe^{3+} redox potential to 3.90 V as well as the underlying structural relationship between the tavorite and triplite phases. Although caution must be exercised because discrete M–O distances cannot be distinguished owing to the atomic disorder in triplite, one may speculate that the increased average M–O bond length (which will reduce the covalent character of the Fe–O bonds) or the fluorine sitting in a *cis* rather than a *trans* configuration may be feasible explanations for the increased redox potential. With respect to the structure, the tavorite and triplite phases do not initially seem to be structurally related; however, on closer examination it can be seen that they are strikingly similar.

The common feature between the two phases is based on an underlying sublattice of SO_4 tetrahedra, which is close-packed along the $[10\bar{1}]$ direction in tavorite and the [100] direction in triplite. If one considers a displacement of the transition metals away from the centre of their octahedra towards the equatorial edges where Li sits, as illustrated in Fig. 6a,c, this would correspond to a shift to an adjacent interstitial. If this mixing of interstitials is done at random,

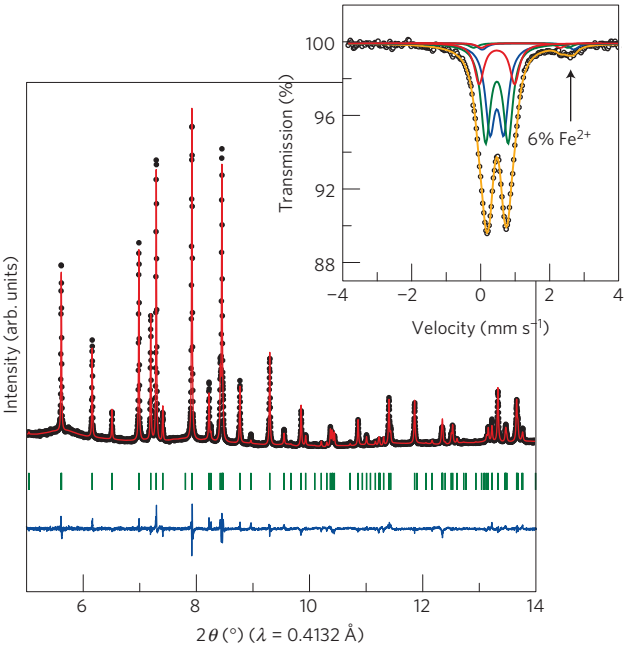

Figure 5 | Synchrotron XRD Rietveld refinement of the chemically oxidized $Li_{0.25}(Fe_{0.8}Mn_{0.2})SO_4F$ sample. There is a volume change of approximately 0.6% between the lithiated and delithiated phases with $R_{Bragg} = 5.92\%$ and $R_f = 5.83\%$. (Black dots correspond to observed data, the orange lines are the calculated patterns, the blue lines are the difference between the calculated and observed patterns and the vertical green bars correspond to the expected positions of Bragg reflections.) The inset shows the Mössbauer spectrum of a fully chemically oxidized sample of nominal composition $Li_{0.25}(Fe_{0.8}Mn_{0.2})SO_4F$ and corresponds to nearly all of the Fe in the 3+ oxidation state. The Mössbauer parameters of the chemically and electrochemically delithiated phases (Fig. 4b) are found to be similar, within experimental uncertainties, indicating the formation of the same phase regardless of the oxidation method. As before, Mössbauer spectra of the lithiated triplite phases show three types of Fe^{2+} environment.

the result would easily explain the 50/50 occupancy of the two sites observed in triplite. These newly occupied interstitials would then result in a distortion of the corner-sharing MO_4F_2 octahedra of tavorite into the highly irregular edge-sharing chains found in triplite with minimal rearrangement of the anionic sublattice, as illustrated in Fig. 6b,d. This structural relationship motivated us to further examine the influence of the synthesis conditions on the search for parameters, which could trigger the nucleation of one polymorph with respect to the other.

It is well known that anatase can be stabilized over rutile TiO_2 at a low temperature when nanoscale powders are prepared[20]. This stabilization is rooted in surface energy contributions that can override thermodynamic considerations when considering only the bulk. With respect to the polymorphs studied here, the ceramic and ionothermal processes use the exact same precursors reacted at the same temperature and pressure, with only the ionic liquid distinguishing the two preparations. As illustrated in the inset of Fig. 1b,d, the presence of ionic liquid results in nanoscale powders, compared with the micrometre-sized powders for the ceramic route. Therefore, the particle size could reasonably be a determining factor in the growth of tavorite versus triplite in ionic liquid. To investigate this possibility, the reaction time of the ionothermal process was extended to favour particle coarsening. Reaction times of one day were found to yield pure tavorite phase, whereas times of one week and two weeks were found to both yield a mixture of phases with a maximum of 75% by mass consisting of the triplite phase. It should also be noted that we cannot completely rule out the

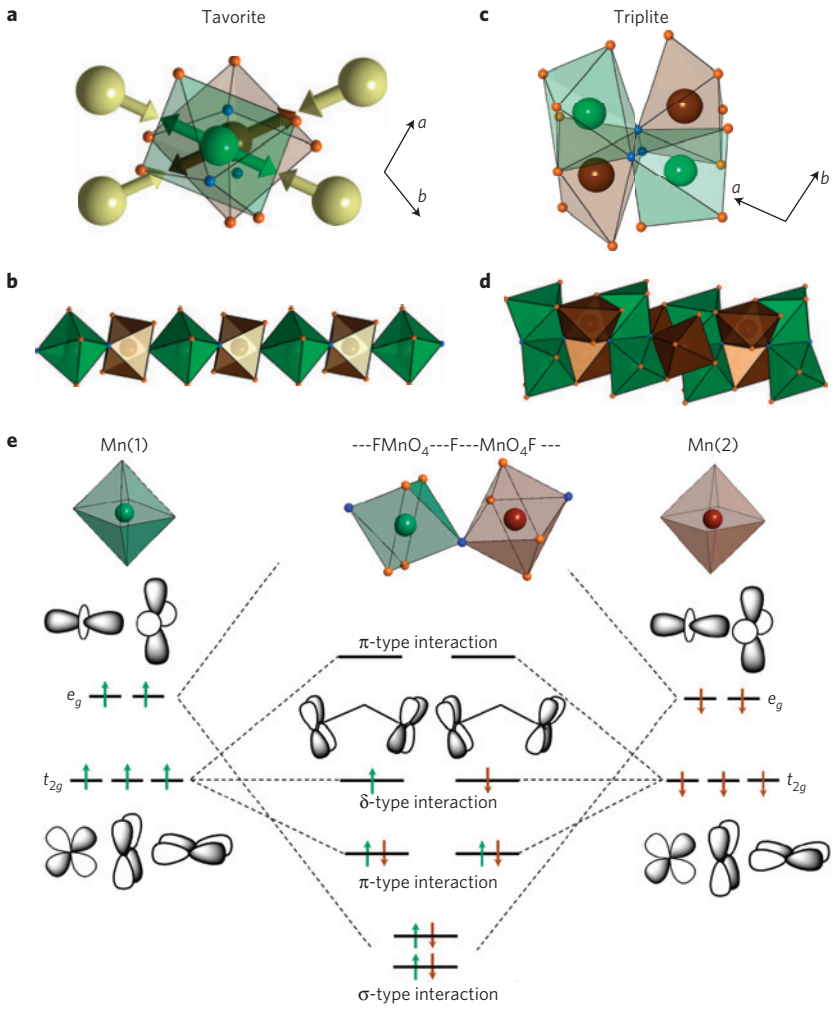

Figure 6 | Structural relationship between the tavorite and triplite phases. a–d, Segments of the structure illustrating the location of the metal and Li atoms in relation to the chain direction. The green and brown octahedra correspond to sites 1 and 2 of the triclinic structure, with yellow spheres illustrating the Li ions. If the transition metal atoms are displaced from the centre of their octahedra towards the edges, as illustrated by the arrows in **a**, one can imagine building up the triplite structure, which is illustrated in **c** and **d**. **e**, A qualitative representation of the orbital splitting expected along the chain between two corner-sharing octahedra, where only the localized metallic orbitals are shown. The σ-, π- and δ-type interactions refer to the metal–metal orbital overlap and the relative energies of the e_g- versus t_{2g}-like electronic levels have been determined through first-principles calculations (see Supplementary Table S9).

role water may play in modifying the nucleation–growth kinetics of one polymorph with respect to the other because the two routes are differentiated by whether water is trapped as a liquid or quickly released as a vapour.

As a way to further probe the stability of these two polymorphs, first-principles density functional theory (DFT) +U calculations were conducted that confirmed the close thermodynamics (within thermal energy $k_B T$), independent of the magnetic arrangement considered in the calculations (see Supplementary Table S9). However, local chemical bonding and orbital analyses are more pertinent descriptors to rationalize the metastability of the tavorite phase in the case of Mn. Figure 6e illustrates the orbital interactions occurring along the tavorite chains between two consecutive MO_4F_2 octahedra. From this diagram, an electronic instability (half-filling) is clearly associated with the δ-type orbitals for Mn (fully filled for Fe), which was further confirmed by DFT calculations (Supplementary Fig. S8). To stabilize such a configuration and split the degeneracy of the δ-type orbitals, local distortions must occur. This can be achieved through the closing of the M–F–M angle along the tavorite chains to form edge-sharing octahedra (see Fig. 6d), as found in the triplite structure. From this analysis, one may consider that any electronic perturbation associated with the creation of holes in the Fe-based band of the tavorite structure could trigger the tavorite to triplite phase transition leading to the possibility that non-stoichiometric $LiFeSO_4F$ may crystallize in the triplite structure.

Last, first-principles calculations that have successfully predicted the redox voltage of tavorite (3.60 V; refs 21–23) were extended to study the triplite $Li_x(Fe_{1-\delta}Mn_\delta)SO_4F$ phases neglecting disorder. Using this assumption, the experimental trends are well reproduced, leading to potentials around 4.0 V and showing that only Fe is involved in the redox process. However, work is still in progress to quantify the effect of disorder on the computed voltages.

We now turn to the question of why, despite the fact that there is no open void space to allow for ionic diffusion, triplite seems to demonstrate a nicely reversible and high-capacity Li insertion process. The tavorite phase of $LiFeSO_4F$, having an open-framework structure, was demonstrated experimentally and theoretically to be a three-dimensional lithium-ion conductor[24,25]. In contrast, if one assumes that the triplite-phase inherits the atomic disorder present in the $LiMnSO_4F$, such three-dimensional conductivity should not be possible. As illustrated in Fig. 2b, a

preferential segregation of the Fe from the Li and Mn atoms between sites 1 and 2 would open channels for Li to move (for example, percolating paths). Although, this could offer an explanation for why samples containing Mn content in excess of 40%, schematically represented by the insets of Fig. 2a, fail to deliver electrochemical activity as Mn obstructs the channels (for example, loss of percolation for Li ions), caution must be exercised as coupled neutron and synchrotron experiments are truly needed to ascertain precise site occupancies.

Although open channels provide energetically favourable pathways for fast lithium ion diffusion, they are not mandatory. This is clearly supported by the recently reported Li insertion–extraction processes in Li_2FeSiO_4, which also exhibits several polymorphs[26]. It can easily be imagined that a Li ion changes direction each time it encounters a transition-metal atom, which would lead to some displacements and the creation of some random zigzag pathways in the structure. Such displacement is conceivable in polymorphs that are close in energetic stability and are therefore prone to site mixing for entropic reasons. To definitively identify the real Li conduction pathway, atomistic modelling is absolutely necessary.

Mn substitution for Fe in $Li(Fe_{1-\delta}Mn_\delta)SO_4F$ was found to trigger a transformation from the tavorite to the triplite structure, with a resulting increase of 300 mV in the Fe^{2+}/Fe^{3+} redox potential. These Fe-rich triplite phases constitute a new class of electrode materials, among which the $\delta = 0.05$ and 0.10 compositions are the most attractive because they exhibit reversible capacities of nearly 0.8 Li^+ per formula unit at 3.90 V, with good capacity retention and nearly zero volume change (0.6%) between the charged and discharged state. Once the electrode formulation is fully optimized, such an electrode material could become a serious contender to $LiFePO_4$, as its theoretical energy density is nearly identical. Its slightly lower theoretical specific capacity (146 mA h g^{-1}), compared with 170 mA h g^{-1} for $LiFePO_4$, is compensated by its higher cell voltage (3.90 V, compared with 3.45 V). Moreover, the synthesis of the triplite phase is relatively cost effective, as it does not require temperatures above 350 °C and the electrode processing uses standard approaches. Besides this practical aspect, such results should capture our interest for metastable materials as a source of unusual properties. These new types of polyanionic compound, having the triplite structure, provide valuable information in the search for even better positive-electrode materials.

Methods

Synthesis. $LiMnSO_4F$ was prepared at a low temperature of 290–300 °C by reacting an equimolar mixture of LiF and $MnSO_4 \cdot H_2O$ through ionothermal synthesis for 24 h or solid-state synthesis for 40–50 h (refs 9,13). To prepare mixed-metal fluorosulphates, various $(Fe_{1-\delta}Mn_\delta)SO_4F \cdot H_2O$ ($\delta = 0.01 \sim 0.9$) monohydrate precursors were made by dissolving stoichiometric amounts of commercial $FeSO_4 \cdot 7H_2O$ (Aldrich, 99%) and $MnSO_4 \cdot H_2O$ in 5 ml of distilled water under nitrogen bubbling, adding a pinch of ascorbic acid to convert any Fe^{3+} salts to Fe^{2+} salts, precipitating the mixed precursor by adding ethanol, drying the recuperated solid and finally heating it either using ionic liquid or under vacuum. This process is described in detail in ref. 10. Later, these monohydrate precursors were mixed with an equimolar amount of LiF by ball-milling (Spex 800) for 15 min. For ionothermal synthesis, ~1 g of precursor mixture was mixed with 5 ml of EMI-TFSI inside a Teflon-lined autoclave, stirred for 20 min before slowly heating to 290–295 °C (at 5 °C min^{-1}) and keeping it at this temperature for 24 h before gradual cooling by switching the furnace off. The reaction product was recuperated by washing the ionic liquid twice with ethyl acetate and drying the powder at 60 °C. For solid-state synthesis, the reaction mixture was uniaxially pressed into pellets, loaded inside a Teflon-lined autoclave (in Ar-filled glove-box), slowly heated to 290–295 °C (5 °C min^{-1}) and annealed for 24–50 h before slow cooling to ambient temperature. The final product was simply ground in a mortar and pestle for further study. Even for the latter route, the reaction is complete in 24 h, as for the ionic liquid route. However, longer annealing was used to obtain well-crystallized products. Polymer-assisted synthesis was carried out, which is very similar to ionothermal synthesis, except that a polymer is used in place of the ionic liquid as the reacting medium. Irrespective of the synthesis route, using Fe^{3+}-free monohydrate precursors and slow initial heating are vital for successful synthesis of Fe^{2+}-containing products. It should also be noted that small quantities of LiF, of the order of 5 wt%, were typically observed as an impurity phase.

XRD, synchrotron and Rietveld refinement. XRD patterns were recorded using either a Bruker D8 or a Bruker D4 diffractometer equipped with a Cu–Kα source operating at 40 kV/40 mA ($\lambda_1 = 1.54053$ Å, $\lambda_2 = 1.54431$ Å) and a LynxEye detector. Synchrotron powder diffraction patterns were collected in the Swiss–Norwegian Beam Lines at the European Synchrotron Radiation Facility in Grenoble (France). Additional high-resolution synchrotron powder diffraction data were collected using beamline 11-BM at the Advanced Photon Source, Argonne National Laboratory, using an average wavelength of around 0.4132 Å. Discrete detectors covering an angular range from −6 to 16° 2θ are scanned over a 34° 2θ range, with data points collected every 0.001° 2θ and a scan speed of 0.01° s^{-1}. The powder patterns were refined using the Rietveld method with the FullProf program (ref. 17), starting with atomic coordinates as determined by FOX (ref. 27). Temperature-controlled XRD in air was conducted in a Bruker D8 diffractometer equipped with an HTK 1200 °C Anton Paar chamber. The powder patterns were collected for ~25 min at any temperature (varying from room temperature to 600 °C) in the 2θ range of 15°–50°.

Mössbauer spectroscopy. ^{57}Fe Mössbauer spectra were recorded in the transmission geometry in the constant acceleration mode and with a ^{57}Co(Rh) source with a normal activity of 925 MBq. The velocity scale (±4 mm s^{-1}) was calibrated at room temperature with α-Fe foil. The absorbers were prepared from 50 mg of powder. The hyperfine parameters δ (isomer shift) and ΔE_q (quadrupole splitting) were determined by fitting Lorentzian lines to the experimental data using the MOSFIT program[28]. The isomer shift values are calculated with respect to that of α-Fe.

EXAFS measurements. X-ray absorption spectroscopy studies in quick extended X-ray absorption fine structure (QEXAFS) and XANES modes were carried out at the Diamond Light Source, UK. The samples were characterized using the core EXAFS beamline B18, which covers a wide energy range (2.05–35 keV) and is equipped with a double-crystal monochromator containing two pairs of crystals, Si(111) and Si(311), optimized for QEXAFS measurements[29]. The short-range structural information available using QEXAFS and XANES methods, coupled with the time resolution offered by B18, allowed for the determination of changes in the Fe and Mn oxidation states. The monochromator was calibrated using an iron or manganese foil, depending on the edge under investigation. Fe and Mn K-edge transmission spectra were collected for all samples, together with several iron and manganese standards. EXAFS spectra were background subtracted, splined and analysed using SIXPack (ref. 30). The data were collected with a step size of less than 0.5 eV and all samples were measured at ambient temperature.

For *in situ* studies, a stainless-steel Swagelok-style cell fitted with an X-ray-transparent Be window was employed to monitor the battery cell in operando[31]. An aluminium foil covered the Be window to prevent oxidation at higher operating voltages. The cathode material, mixed with 15 wt% carbon, was loaded directly onto the Be window. Lithium metal was used as the negative electrode and a fibre separator soaked in 1 M LP30 acted as the electrolyte.

TGA, SEM and TEM. Thermogravimetric analysis (TGA) was carried out on powder samples in the temperature range 30–800 °C (heating rate = 10 °C min^{-1}, in air) using a Simultaneous Thermal Analyser STA-449C Jupiter unit (Netzsch). Scanning electron microscopy (SEM) was conducted using an FEI Quanta 200 F field-emission scanning electron microscope (20 kV) operating under low-vacuum conditions to avoid the charging effect. Elemental analysis was carried out at several spots to ensure a homogeneous distribution of all elements. Transmission electron microscopy (TEM) was carried out using an FEI Tecnai F20 S-Twin electron microscope (200 kV). The powders were dispersed in high-purity acetone and were deposited on a holey carbon-coated copper TEM grid for TEM imaging.

Inductively coupled plasma. Measurements were carried out for the chemically oxidized Fe-rich ($\delta = 0.2$) sample. A lithium content of 0.25(1) was found, giving a nominal composition of $Li_{0.25}(Fe_{0.8}Mn_{0.2})SO_4F$, indicative of an efficient oxidation process with 0.75 Li^+ extracted. In parallel, Mössbauer experiments (inset of Fig. 5) indicate the presence of 96% Fe^{3+} (Supplementary Table S8), implying that 0.768 (0.96 × 0.8) Fe^{2+} have been oxidized, perfectly matching within the accuracy of the measurements the amount of Li removed. Combining these two numbers further demonstrates that only Fe undergoes oxidation and that none of the Mn is oxidized. Furthermore, the delithiated $Li_{0.25}(Fe_{0.8}Mn_{0.2})SO_4F$ phase was found to demonstrate the same thermal stability as the parent phase up to 345 °C, as determined by *in situ* high-temperature XRD and TGA measurements (Supplementary Figs S4 and S5).

Electrochemical test. The $Li(Fe_{1-\delta}Mn_\delta)SO_4F$ powders were mixed with SuperP carbon black in an 80:20 wt% ratio and were milled for 10 min (Spex 800) in an Ar atmosphere. Standard Swagelok-type cells were assembled using the above active materials as a positive electrode and Li metal foil as a negative electrode, separated by two sheets of Whatman GF/D borosilicate glass fibre saturated with 1 M $LiPF_6$ solution in a 1:1 w/w mixture of ethylene carbonate/dimethyl carbonate as the electrolyte. Usual cathode loading was 7–10 mg cm^{-2} per cell. The cells were assembled inside an Ar-filled glove box and were subjected

to galvanostatic charge–discharge cycling (at 20 °C) using a Mac-Pile system (Biologic, S.A.). The cells were typically cycled between 2.5 and 4.5 V versus Li at 1 Li^+ exchanged per 20 h.

Received 3 May 2011; accepted 7 July 2011; published online 21 August 2011

References

1. Armand, M. & Tarascon, J-M. Building better batteries. *Nature* **451,** 652–657 (2008).
2. Tarascon, J-M. & Armand, M. Issues and challenges facing rechargeable lithium batteries. *Nature* **414,** 359–367 (2001).
3. Yamada, A. *et al.* Lithium iron borates as high capacity battery electrodes. *Adv. Mater.* **22,** 3583–3587 (2010).
4. Nyten, A., Abouimrane, A., Armand, M., Gustafsson, T. & Thomas, J.O. Electrochemical performance of Li_2FeSiO_4 as a new Li-battery cathode material. *Electrochem. Commun.* **7,** 156–160 (2005).
5. Nishimura, S. *et al.* Structure of Li_2FeSiO_4. *J. Am. Chem. Soc.* **130,** 13212–13213 (2008).
6. Nishimura, S., Makamura, M., Natsui, R. & Yamada, A. New lithium iron pyrophosphate as 3.5 V class cathode material for lithium ion battery. *J. Am. Chem. Soc.* **132,** 13596–13597 (2010).
7. Barker, J., Saidi, M. Y. & Swoyer, J. L. A comparative investigation of the Li insertion properties of the novel fluorophosphate phases, $NaVPO_4F$ and $LiVPO_4F$. *J. Electrochem. Soc.* **151,** 1670–1677 (2004).
8. Padhi, A. K., Nanjundaswamy, K. S. & Goodenough, J. B. Tuning the position of the redox couples in materials with NASICON structure by anionic substitution. *J. Electrochem. Soc.* **145,** 1518–1520 (1998).
9. Recham, N. *et al.* A 3.6 V lithium-based fluorosulphate insertion positive electrode for lithium-ion batteries. *Nature Mater.* **9,** 68–74 (2010).
10. Barpanda, P. *et al.* Structure and electrochemical properties of novel mixed $Li(Fe_{1-x}M_x)SO_4F$ (M = Co, Ni) phases fabricated by low temperature ionothermal synthesis. *J. Mater. Chem.* **20,** 1659–1668 (2010).
11. Rea, J. R. & Kostiner, E. The crystal structure of manganese fluorophosphate, $Mn_2(PO_4)F$. *Acta Crystallogr. B* **28,** 2525–2529 (1972).
12. Recham, N. *et al.* Ionothermal synthesis of tailor-made $LiFePO_4$ powders for Li-ion battery applications. *Chem. Mater.* **21,** 1096–1107 (2009).
13. Ati, M. *et al.* Fluorosulphate positive electrodes for Li-ion batteries made via a solid-state dry process. *J. Electrochem. Soc.* **157,** 1007–1015 (2010).
14. Barpanda, P. *et al.* Structural and electrochemical investigation of novel $AMSO_4F$(A = Na, Li; M = Fe, Co, Ni, Mn) metal fluorosulphates prepared using low temperature synthesis routes. *Inorg. Chem.* **49,** 7401–7413 (2010).
15. Barpanda, P. *et al.* $LiZnSO_4F$ made in an ionic liquid: A new ceramic electrolyte composite for solid-state Li-batteries. *Angew. Chem. Int. Ed.* **50,** 2526–2531 (2010).
16. Ati, M. *et al.* Fluorosulfate positive electrode materials made with polymers as reacting media. *Electrochem. Solid-State. Lett.* **13,** 150–153 (2010).
17. Rodríguez-Carvajal, J. Recent advances in magnetic structure determination by neutron powder diffraction. *Physica B* **192,** 55–69 (1993).
18. Shannon, R. D. & Prewitt, C. T. Effective ionic radii in oxides and fluorides. *Acta. Cryst* **B25,** 925 (1969).
19. Tarantino, S. C., Ghigna, P., McCammon, C., Amantea, R. & Carpenter, M. A. Local structure properties of $(Mn, Fe)Nb_2O_6$ from Mössbauer and X-ray absorption spectroscopy. *Acta Cryst. B* **61,** 250–257 (2005).
20. Hanaor, D. & Sorrell, C. Review of the anatase to rutile phase transformation. *J. Mater. Sci.* **46,** 1–20 (2011).
21. Frayret, C. *et al.* $LiMSO_4F$ (M = Fe, Co, and Ni): Promising new positive electrode materials through the DFT microscope. *Phys. Chem. Chem. Phys.* **12,** 15512–15522 (2010).
22. Cai, Y. *et al.* First-principles calculations on the $LiMSO_4F/MSO_4F$ (M = Fe, Co, and Ni) systems. *J. Phys. Chem. C* **115,** 7032–7037 (2011).
23. Ramzan, M., Lebegue, S., Kang, T. W. & Ahuja, R. Hybrid density functional calculations and molecular dynamics study of lithium fluorosulphate, a cathode material for lithium-ion batteries. *J. Phys. Chem. C* **115,** 2600–2603.
24. Tripathi, R., Gardiner, G. R., Islam, M. S. & Nazar, L. F. Alkali-ion conduction paths in $LiFeSO_4F$ and $NaFeSO_4F$ tavorite-type cathode materials. *Chem. Mater.* **23,** 2278–2284 (2011).
25. Liu, Z. & Huang, X. Structural, electronic, and Li diffusion properties of $LiFeSO_4F$. *Solid State Ion.* **181,** 57–61 (2010).
26. Sirisopanaporn, C., Masquelier, C., Bruce, P., Armstrong, A. & Dominko, R. Dependence of Li_2FeSiO_4 electrochemistry on structure. *J. Am. Chem. Soc.* **133,** 1263–1265 (2011).
27. Favre-Nicolin, V. & Cerny, R. Fox, 'free objects for crystallography': A modular approach to *ab initio* structure determination from powder diffraction. *J. Appl. Cryst.* **35,** 734–743 (2002).
28. Varret, F. & Teillet, J. *Unpublished Mosfit Program* (Universite du Maine, 1976).
29. Dent, A. J. B18: A core XAS spectroscopy beamline for diamond. *J. Phys. Conf. Ser.* **190,** 012039 (2009).
30. Webb, S. M. SIXPack: A graphical user interface for XAS analysis using IFEFFIT. *Phys. Scr.* **T115,** 1011–1014 (2005).
31. Leriche, J. B. *et al.* An electrochemical cell for operando study of lithium batteries using synchrotron radiation. *J. Electrochem. Soc.* **157,** A606–A610 (2010).

Acknowledgements

Many discussions with M. Armand, N. Recham, C. Delacourt, C. Masquelier, D. Larcher, G. Férey, Y. Chabre, C. Frayret and D.W. Murphy are gratefully acknowledged. We thank C. Davoisne for the TEM images and ALISTORE-ERI for sponsoring this research. Use of the Advanced Photon Source at Argonne National Laboratory was supported by the US Department of Energy, Office of Science, Office of Basic Energy Sciences, under Contract No. DE-AC02-06CH11357. The EXAFS measurements were carried out with the support of the Diamond Light Source and we gratefully acknowledge G. Cibin for help with running the X-ray absorption spectroscopy experiments as well as E. J. Schofield and A. V. Chadwick for discussions in analysing the XANES data.

Author contributions

P.B., M.A. and J-M.T. carried out the synthesis, the electrochemical work and designed the research approach; B.C.M., G.R. and J-N.C. analysed the crystal structure and diffraction patterns; M.T.S. and J-C.J. collected the Mössbauer measurements; B.C.M. and S.A.C. collected and analysed the EXAFS measurements; M-L.D. conducted the DFT calculations and developed the theoretical framework; B.C.M., G.R. and J-M.T. wrote the manuscript and all authors discussed the experiments and final manuscript.

Additional information

The authors declare no competing financial interests. Supplementary information accompanies this paper on www.nature.com/naturematerials. Reprints and permissions information is available online at http://www.nature.com/reprints. Correspondence and requests for materials should be addressed to J.M.T.